

Ultrafast Electron Injection Dynamics of Photoanodes for Water-Splitting Dye-Sensitized Photoelectrochemical Cells

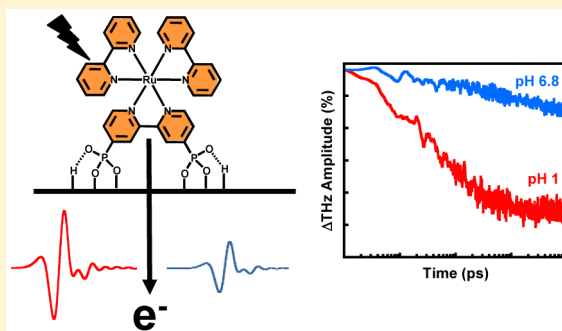
John R. Swierk,^{†,⊥} Nicholas S. McCool,^{‡,⊥} Coleen T. Nemes,[†] Thomas E. Mallouk,^{*,‡,§,||} and Charles A. Schmuttenmaer^{*,†}

[†]Department of Chemistry and Energy Sciences Institute, Yale University, 225 Prospect Street, P.O. Box 208107, New Haven, Connecticut 06520-8107, United States

[‡]Department of Chemistry, [§]Department of Biochemistry and Molecular Biology, and ^{||}Department of Physics, The Pennsylvania State University, University Park, Pennsylvania 16802, United States

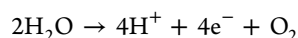
Supporting Information

ABSTRACT: Efficient conversion of solar energy into useful chemical fuels is a major scientific challenge. Water-splitting dye-sensitized photoelectrochemical cells (WS-DSPECs) utilize mesoporous oxide supports sensitized with molecular dyes and catalysts to drive the water-splitting reaction. Despite a growing body of work, the overall efficiencies of WS-DSPECs remain low, in large part because of poor electron injection into the conduction band of the oxide support. In this study, we characterize the ultrafast injection dynamics of several proposed oxide supports (TiO_2 , $\text{TiO}_2/\text{Al}_2\text{O}_3$, SnO_2 , $\text{SnO}_2/\text{TiO}_2$) under identical conditions using time-resolved terahertz spectroscopy. In the absence of an Al_2O_3 overlayer, we observe a two-step injection from the dye singlet state into nonmobile surface traps, which then relax into the oxide conduction band. We also find that, in SnO_2 -core/ TiO_2 -shell configurations, electron injection into TiO_2 trap states occurs rapidly, followed by trapped electrons being released into SnO_2 on the hundreds of picoseconds time scale.



1. INTRODUCTION

In the search for a renewable energy alternative to fossil fuels, solar energy is perhaps the most promising alternative. Despite significant solar irradiance ($\sim 120\,000$ TW impinging on the Earth),¹ capturing and storing this abundant solar energy remains a significant challenge. Natural photosynthesis suggests a possible solution to this challenge: utilize a series of ultrafast electron transfers between spatially separated components to harvest light, convert it to useful potential energy, and finally store that potential energy in reduced carbon products.² Artificial photosynthetic systems aim to mimic natural photosynthesis by oxidizing water at an anode via



to generate protons and electrons, which are subsequently reduced at a cathode to produce molecular hydrogen, or in tandem with CO_2 to yield a reduced carbon fuel. Molecular oxygen is also produced at the anode as a byproduct of the water-splitting reaction, and it is this kinetically slow process that often limits overall efficiency in artificial photosynthetic systems.

Characterizing the myriad of electron transfer events that occur in a functioning artificial photosynthetic device is a significant analytical challenge. Events occurring at nanosecond or faster time scales are typically characterized by spectroscopic techniques such as transient absorbance, where changes in

visible or near-IR absorbance are observed. Most artificial photosynthetic systems utilize semiconductor components in which electron dynamics can be difficult to probe with traditional transient absorption techniques because of secondary processes such as luminescence. Even still, at best these techniques can only confirm the presence of an electron in the semiconductor without giving information about its state.³ Unlike visible or near-IR ultrafast techniques, time-resolved terahertz spectroscopy (TRTS) directly probes changes in oxide conductivity related to photoexcitation with sub-picosecond resolution.⁴ Mobile electrons injected into the conduction band attenuate the transmitted terahertz radiation (THz); thus, an increase in conductivity upon photoinjection of electrons is observed as a decrease in the transmitted THz amplitude. This conductivity increase is in turn proportional to the product of the mobility and the carrier density. If the mobility is constant between samples (as when several different dyes on the same metal oxide are compared) then differences in the THz amplitude are directly proportional to carrier density and by extension the relative injection efficiency. When coupled with complementary transient absorption studies, TRTS provides a fuller picture of the electron injection dynamics

Received: January 22, 2016

Revised: February 26, 2016

Published: March 3, 2016

and offers a powerful tool for understanding electron transfer into semiconductors from the perspective of the semiconductor itself.

Water-splitting dye-sensitized photoelectrochemical cells (WS-DSPECs) draw inspiration from biological systems, utilizing molecular dyes anchored to a high surface area metal oxide support to harvest light.⁵ In the most common example, the photoexcited dye injects an electron into the conduction band of a mesoporous TiO₂ film. The electron then percolates through the film to a transparent conducting oxide back contact and is subsequently transported to a dark cathode. On the surface of the TiO₂, a series of fast electron transfers^{6,7} bring the hole to a water oxidation catalyst, which subsequently oxidizes water. Despite numerous examples^{8–22} of WS-DSPECs utilizing a variety of molecular sensitizers and water oxidation catalysts, overall efficiencies remain low under standard one-sun solar irradiance.

A major cause of the low efficiency in WS-DSPECs is the need to balance electron injection against maintaining sufficient overpotential to drive a water oxidation catalyst. Below pH 4, the Ru(III/II) formal potential of the most common ruthenium sensitizer (4,4'-H₂PO₃-bpy)(bpy)₂Ru(II) [bpy = 2,2'-bipyridine, 4,4'-H₂PO₃-bpy = 4,4'-diphosphonato-2,2'-bipyridine] (Ru(II)phos) is too cathodic to drive water oxidation. Unfortunately, Ru(III)(bpy)₃ sensitizers are also susceptible to nucleophilic attack under basic conditions.²³ Thus, WS-DSPECs that utilize Ru(III) polypyridyl sensitizers must operate at or near neutral pH where the injection efficiency of Ru(II)phos is estimated to be a mere 20%.^{24,25} Injection efficiencies of porphyrin sensitizers into TiO₂ is estimated to be even poorer.^{12,26} Of those injected electrons only a small percentage (1–2%) persist at time scales relevant to solar fuel production.²⁵

Although TiO₂ is the best-studied metal oxide semiconductor in WS-DSPECs, others have recently begun to gain attention. Some studies have utilized oxides with more positive conduction band potentials aiming to enhance injection kinetics, while others have utilized core/shell electrodes in an attempt to maintain efficient injection and retard recombination.^{9,17–19} While there are reports utilizing ultrafast transient absorbance to monitor the injection dynamics of Ru(II)phos into TiO₂ and SnO₂,^{21,27} as well as porphyrin sensitizers relevant to WS-DSPECs,^{16,17,26} there are no reports utilizing terahertz spectroscopy. Furthermore, there is as yet little understanding of the dynamics of electrons after their injection into TiO₂ and core/shell structures that are relevant to WS-DSPECs. In addition, preparation and experimental conditions vary greatly among these studies, making direct comparison difficult. In this study, we explore the injection dynamics of Ru(II)phos on several common photoanode designs for WS-DSPECs utilizing TRTS.²⁸ To ensure maximum comparability, all of the mesoporous films are sensitized and measured under identical conditions. TRTS provides new insight into the trapping of photoinjected electrons in WS-DSPECs, which adds to the mechanistic understanding gained from other transient spectroscopic and electrochemical techniques.

2. EXPERIMENTAL SECTION

All reagents were purchased from Sigma-Aldrich or Alfa Aesar and used as received. Bis(2,2'-bipyridine)(4,4'-diphosphonato-2,2'-bipyridine)ruthenium(II) bromide was prepared as previously described.²⁹

2.1. Sample Preparation. TiO₂ (<25 nm) and SnO₂ (22–43 nm) nanoparticles were prepared as a paste for doctor-blading following the method of Ito et al.³⁰ Briefly, the nanoparticles were successively ground with acetic acid, water, and ethanol and then ultrasonicated for 4 min at a 70% duty cycle using an ultrasonic horn. α -Terpineol and ethyl cellulose were added with additional ultrasonication after each addition. Excess ethanol was removed on a rotary evaporator to produce a paste. The films were prepared by doctor-blading on fused quartz substrates (GM Associates) using Scotch tape as a spacer layer. After each layer, the sample was heated at 80 °C for 10 min before application of the next layer. A total of five layers of paste was applied to each sample to give a nominal film thickness of 6 μ m for TiO₂ and 8 μ m for SnO₂. The films were sensitized for 16 h in a 0.1 mM solution of Ru(II)phos in anhydrous ethanol.

Core/shell structures were fabricated using a Savannah atomic layer deposition (ALD) system. As-prepared, sensitized TiO₂ and unsensitized SnO₂ films were placed in a 100 °C ALD chamber, which were ramped to reaction temperature and exposed to alternating pulses of metal oxide precursor and water vapor. Due to the high surface area of the films, each vapor pulse was held in the chamber for 180 s before purging with N₂ for 20 s. Four cycles of Al₂O₃ were deposited on sensitized TiO₂ films using trimethylaluminum as a precursor at a deposition temperature of 130 °C. The pulse sequence utilized alternating pulses of water vapor (0.015 s) and precursor (0.015 s). Forty cycles of TiO₂ were deposited on the unsensitized SnO₂ films using tetrakis(dimethylamido)titanium as the precursor with a deposition temperature of 150 °C and pulse durations of 0.03 and 0.25 s for the water vapor and precursor, respectively. Following the deposition, the SnO₂/TiO₂ electrodes were heated at 450 °C for 30 min. Approximately 0.4 nm of Al₂O₃ and 2.6 nm of TiO₂ were deposited as measured by ellipsometry on a Si wafer.

After sensitization, the samples were sealed using a second piece of fused quartz sandwiching a 60 μ m thick Surlyn spacer (Solaronix). The samples were hot pressed at 250 °C for 45 s to melt the Surlyn. The solvent (either pH 1 HClO₄ or pH 6.8 100 mM potassium phosphate buffer) was introduced via vacuum backfilling through a previously drilled hole in the second piece of fused quartz. To improve the stability of the samples at pH 6.8, the phosphate buffer was briefly purged with nitrogen to remove oxygen prior to filling.³¹ A second piece of Surlyn covered with a microscope coverslip was then used to seal the hole.

Scanning/transmission electron microscopy (S/TEM) and energy dispersive X-ray spectroscopy (EDS) were carried out on an FEI Talos F200X S/TEM instrument.

2.2. Time-Resolved THz Spectroscopy. A detailed description of the spectrometer and the technique is available elsewhere.^{28,32–35} In short, the output of an amplified Ti:sapphire laser (Spectra-Physics), which produces 35 fs pulses centered at 800 nm at a repetition rate of 1 kHz, is split three ways into a THz generation beam, pump beam, and detection beam. The pump beam is frequency doubled to 400 nm and attenuated using a variable neutral density filter to achieve a power of 100 mW (100 μ J/pulse) at a spot size of 10 mm, the beam is then passed through a 5 mm aperture before the sample. The THz generation beam is likewise frequency doubled and both the fundamental and second harmonic are focused in air to generate a plasma.^{36,37} The forward propagating THz pulse generated by the plasma is collimated

and focused using off-axis paraboloidal mirrors. The THz radiation is detected using free-space electro-optic sampling with a ZnTe(110) crystal.³⁸ The instrument response function of the spectrometer was described by a Gaussian function with a full-width at half-maximum (fwhm) of 0.5 ps. Samples with slow dynamics were collected with data acquisition parameters which yielded a time resolution of ~ 0.73 ps. Without considering scattering losses, the pump power used in this study results in the excitation of less than 1% of the sensitizers per pulse within the excitation volume.

The following function was fit to the TRTS scans:

$$\Delta\text{THz} = \left\{ \Delta\text{THz}_0 + \sum_{i=1}^n A_i \left[\exp\left(-\frac{t-t_0}{\tau_i}\right) - 1 \right] \right\} \otimes G(\text{fwhm})$$

where THz_0 is a small prezero baseline offset, n is the number of exponentials included in the fit, t_0 corresponds to the excitation "time-zero," A_i is the amplitude of a given component, and τ_i is the time constant associated with that component, $G(\text{fwhm})$ represents a normalized Gaussian instrument response function, and \otimes represents a convolution.

3. RESULTS AND DISCUSSION

3.1. Injection into TiO₂. Previous work by Xiang et al.²¹ and Giokas et al.²⁷ gave specific attention to the ultrafast injection dynamics of Ru(II)phos into TiO₂. Additional work by others has also considered injection by ruthenium polypyridyl complexes into TiO₂.^{3,39,40} Therefore, we begin by considering the injection of Ru(II)phos into TiO₂.

Figure 1 shows the TRTS traces for Ru(II)phos injection into TiO₂ (Ru(II)phos-TiO₂) at pH 1 and pH 6.8 over short

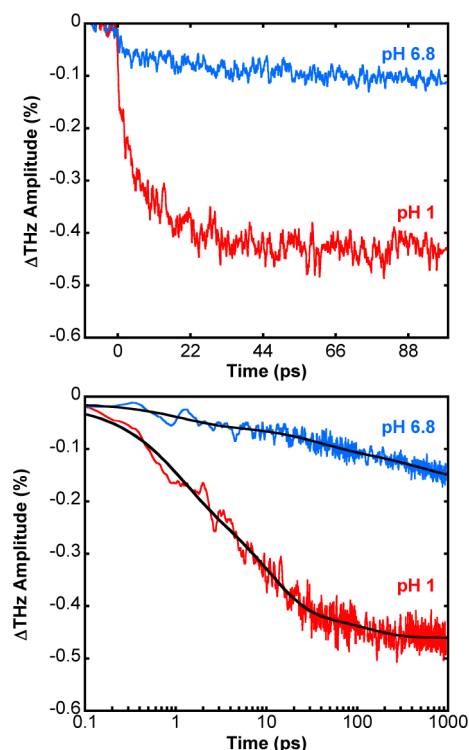


Figure 1. TRTS measurement of Ru(II)phos on TiO₂ at short (upper) and long (lower) time scales in 0.1 M HClO₄ (pH 1, red) and 100 mM potassium phosphate buffer (pH 6.8, blue). Solid black lines are the fitted triexponential functions.

(<100 ps) and longer (950 ps) time scales. It is immediately apparent that the magnitude of the injection into the conduction band changes dramatically from pH 1 to pH 6.8. Assuming the electron mobility in TiO₂ remains constant between these two pH conditions, at 950 ps the injection amplitude (and carrier density) at pH 6.8 is roughly one-third that at pH 1. If the injection efficiency is near unity at pH 1 then that suggests the upper limit of the injection efficiency at pH 6.8 is 33%, which is in good agreement with previous estimates of the injection efficiency.^{24,25}

To fit the TRTS data, we utilized a triexponential function convoluted with a Gaussian instrument response function. This function fit the data well with R^2 values greater than 0.9. Compared to Giokas et al.²⁷ and Xiang et al.,²¹ we observe significantly slower injection kinetics with time constants of 0.7, 9, and 80 ps at pH 1 and 1.3, 33, and 460 ps at pH 6.8 (Table 1). It is also possible that there is an additional slower injection (>1 ns) component that we are unable to resolve with our optical delay stage. After injection we do not see any recovery of the THz amplitude associated with trapping of mobile electrons in sub-bandgap states. Thus, trapping by sub-bandgap trap states must occur on time scales longer than ~ 1 ns.

Probing in the mid-IR region, Xiang et al.²¹ observed a sub-picosecond component, as well as a pair of components with 11 and 150 ps lifetimes. The sub-picosecond component accounted for 63% of the injection amplitude, while the process with the 150 ps time constant only accounted for 9% of the injection amplitude. It is worth noting that the samples in that study were in air, while our samples were sealed with solvent. Also, in the mid-IR free carriers and trapped electrons in the semiconductor are both detected. Of more direct comparability, Giokas et al.²⁷ observed injection via transient absorbance at pH 6.7 and found that 59% of the injection occurred within 1 ps, with the remaining 41% injection occurring on a 250 ps time scale. By comparison, we find that only 18% of the injection amplitude is related to the 1.3 ps time constant.

The differences in injection kinetics may be explained by a number of factors. The solvent used for dye deposition can influence electron transfer kinetics, even under identical measurement conditions.²⁴ Interfacial electron transfer kinetics on nanocrystalline metal oxides are significantly influenced by the surface chemistry and defects of the nanoparticle, which may be different from study to study. It is also important to note that previous studies of the injection of Ru(II)phos into TiO₂ were sensitive to changes in the dye absorbance²⁷ and presence of an electron in TiO₂,²¹ while in this study we observe mobile electrons (i.e., electrons in the conduction band of TiO₂). The discrepancy between transient absorbance measurements (>50% injection occurring within 1 ps) and TRTS measurements (17% of electrons in conduction band within 1 ps) suggests that at least some of the electron injection in WS-DSPECs follows a two-step process: (1) electrons are rapidly injected into nonmobile TiO₂ states, which are invisible to THz radiation, before (2) decaying into mobile conduction band states.

A two-stage injection process is not without precedent. Working with sensitized ZnO, Furube and co-workers^{41,42} observed that the formation of the dye radical cation occurred on a much faster time scale than the appearance of mobile charges in the conduction band. They suggest that initially an exciplex is formed between the dye and a surface state, which later decays as electrons are transferred into the conduction

Table 1. Fit parameters for Figures 1, 3, 4, and 6

oxide	pH	A_1^a	τ_1 (ps)	A_2^a	τ_2 (ps)	A_3^a	τ_3 (ps)	A_4^a	τ_4 (ps)	THz ₀	τ_0 (ps)	fwhm (ps) ^b	scaling factor
TiO ₂	1	0.54	0.7	0.36	9.0	0.10	79.8			0.00	-1.1	0.73	-0.65
	6.8	0.18	1.3	0.36	33	0.47	460			0.00	-0.5	0.73	-0.12
TiO ₂ /Al ₂ O ₃	6.8	0.43	< 0.5	0.17	26	0.40	547			0.00	0.1	0.5	-0.16
SnO ₂	1	0.32	1.7	0.50	9.4	0.18	37.4			0.00	0.0	0.73	-1.2
	6.8	0.23	7.7	0.62	50	0.15	435			0.01	-1.3	0.73	-1.2
SnO ₂ /TiO ₂	1	0.13	< 0.5	-0.12	1.4	0.49	98	0.38	388	0.00	0.0	0.5	-0.67
	6.8	0.20	< 0.5	-0.23	1.1	0.23	95	0.57	430	0.00	0.0	0.5	-0.39

^a A_1 , A_2 , A_3 , and A_4 are normalized amplitudes. ^bThe fwhm value was fixed during the fit.

band. It is possible that the discrepancy between the fast injection observed by transient absorbance and the slow appearance of mobile electrons observed by THz in this study may be related to such a phenomenon.

From the standpoint of a functioning WS-DSPEC, the slow kinetics in near-neutral conditions has important implications regarding device performance. Knauf et al. studied the recombination kinetics of Ru(II)phos and found that a significant fraction of injected electrons recombined on the tens of nanoseconds time scale.⁴³ This suggests that under the best conditions recombination may only be one or two orders of magnitude slower than the slow injection component and at worst may be occurring to some extent on the same time scale. For comparison, in dye-sensitized solar cells, which exhibit significantly better power conversion efficiencies than WS-DSPECs, the injection kinetics are 6–7 orders of magnitude faster than the major recombination pathway.⁴⁴

3.2. Injection into TiO₂/Al₂O₃. Stabilizing dye-sensitized electrodes for long-term operation in oxygen-saturated conditions is an important goal for WS-DSPEC research. Recently Meyer and co-workers have introduced the so-called “mummy” strategy^{45–47} whereby the sensitized metal oxide is covered by a metal oxide overlayer using ALD. With the presence of an overlayer, the desorption rate constant can be decreased by nearly an order of magnitude relative to the uncoated films, offering a significant enhancement in long-term stability. Overlayers of Al₂O₃ are grown via a reaction of vapor phase AlMe₃ and hydroxyl groups on the surface of TiO₂ to generate Ti–O–AlMe₂ and subsequently converted to Ti–O–Al(OH)₂ with the addition of water vapor.⁴⁵ Figure S1 shows that in the presence of Al₂O₃ there is slight broadening and red shift of the MLCT, however, there does not appear to be a significant loss of sensitizers following the ALD treatment.

Hanson et al.⁴⁵ briefly explored the interfacial electron transfer of a TiO₂ film sensitized with Ru(II)phos and coated by overlayers of Al₂O₃ of varying thicknesses. They found that as the overlayer thickness increased, both the rate of back electron transfer and the electron injection efficiency decreased, suggesting deposition of Al₂O₃ between the dye and TiO₂. Using a slightly modified procedure, we deposited an ~0.4 nm overlayer on a Ru(II)phos-sensitized TiO₂ film (Al₂O₃-Ru(II)phos-TiO₂). The Al₂O₃ layer is conformal (Figure 2) and uniform throughout the TiO₂ film.

To avoid acid hydrolysis of the Al₂O₃, we performed TRTS on Al₂O₃-Ru(II)phos-TiO₂ only at pH 6.8 (Figure 3). With a nominally identical sample, Hanson et al.⁴⁵ showed a 25% loss of injection efficiency with the introduction of the Al₂O₃ overlayer. Contrary to those results, we observe that at 950 ps the injection amplitudes are nearly identical between Al₂O₃-Ru(II)phos-TiO₂ and Ru(II)phos-TiO₂. This suggests that the Al₂O₃ overlayer may attenuate a slow injection process beyond

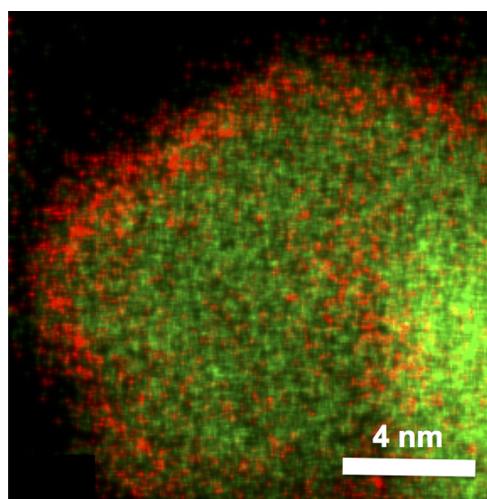


Figure 2. High resolution EDS mapping of TiO₂ particles with an ~0.4 nm overlayer of Al₂O₃. Aluminum is colored red, and titanium is colored green.

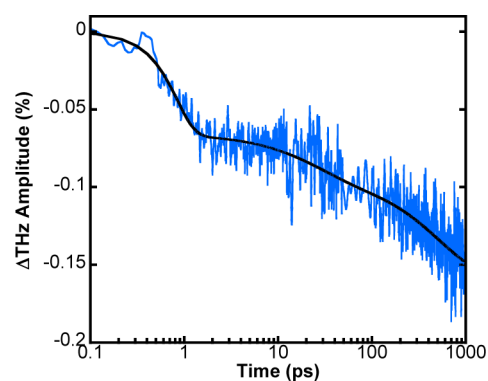


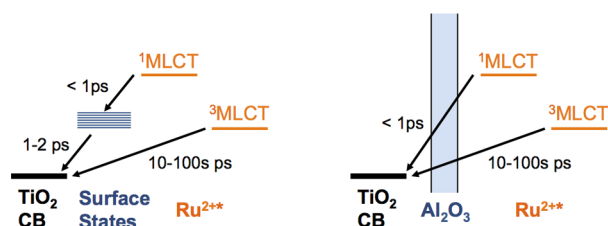
Figure 3. TRTS measurement of Al₂O₃-Ru(II)phos-TiO₂ in 100 mM potassium phosphate buffer (pH 6.8, blue). Solid black line is the fitted triexponential function.

the time scale we can observe. To gain insight into the electron injection kinetics, we fit a convoluted triexponential function to the TRTS scans of the Al₂O₃-coated sample, which yielded a fast, instrument response limited time constant of less than 0.5 ps as well as longer time constants of 25 and 545 ps (Table 1). There is a notable difference in the relative injection amplitudes between the two samples. In the uncoated TiO₂ sample, approximately 18% of the injection amplitude was related to injection on the ~1 ps time scale. With an overlayer of Al₂O₃, nearly 43% of the injection amplitude is associated with the 0.4 ps time constant, which is more consistent with the results of Giokas et al.²⁷ and Xiang et al.²¹

Injection into TiO₂ with ruthenium polypyridyl dyes can occur via a “hot injection” from the singlet state, ¹MLCT, or can occur from the relaxed triplet state, ³MLCT, which is properly described as a manifold of triplet states. Injection from the ¹MLCT state is rapid and generally occurs on sub-picosecond time scales.^{39,40} In this and in previous studies,^{21,27} the fast injection component can be reasonably assigned to dye molecules in the ¹MLCT state, while the slower components are generally assigned to injection from the triplet manifold.

In the presence of an Al₂O₃ overlayer, we see a better than twofold enhancement in the number of electrons appearing in the conduction band within 1 ps. We propose that this enhancement in the fast injection component is related to passivation of surface states that can act as nonmobile trap states (Scheme 1). Hupp and co-workers,⁴⁸ who studied

Scheme 1. Proposed Injection Scheme for Bare (Ru(II)phos-TiO₂) and Al₂O₃ Overlaid (Al₂O₃-Ru(II)phos-TiO₂) Samples^a



^aFor bare samples, injection from the singlet (¹MLCT) proceeds through nonmobile surface states, which subsequently decay into the conduction band (TiO₂ CB). In the presence of the Al₂O₃ overlayer, injection proceeds directly from ¹MLCT to the conduction band.

electron tunneling behavior through metal oxide shells deposited by ALD, found that a single ALD cycle of TiO₂ on a SnO₂ particle could significantly slow the rate of electron transfer from the SnO₂ conduction band to an I₃⁻ acceptor in solution. Their interpretation was that this single ALD cycle passivated surface states that facilitated electron transfer into solution. We suggest that the same phenomenon may be responsible for the enhancement of the fast injection component in Al₂O₃-coated sample: injection from ¹MLCT proceeds directly into the conduction band of TiO₂ without going through a surface intermediate. Because the slower time constants (likely related to injection from the ³MLCT) are relatively unaffected by the Al₂O₃, we can speculate that the energies of the nonmobile surface states lay above that of the ³MLCT. A more detailed study is needed to confirm this proposed injection mechanism.

3.3. Injection into SnO₂. Few sensitizers are able to attain the sufficiently positive ground state potential required to drive a water oxidation catalyst at neutral pH. Furthermore, of those molecules that can drive water oxidation, even fewer possess an excited state sufficiently negative to transfer an electron into TiO₂. With a conduction band 500 mV more positive than TiO₂ and a higher electron mobility, SnO₂ has recently gained attention as an intriguing alternative to TiO₂ in WS-DSPECs.²⁶ Despite these desirable qualities, electron injection into SnO₂ is notoriously slow; this effect is generally attributed to a low density of conduction band states in SnO₂.^{49,50}

Figure 4 shows the TRTS traces for Ru(II)phos injection into SnO₂ (Ru(II)phos-SnO₂) at pH 1 and pH 6.8 on both short and long time scales. As with TiO₂, the injection is more

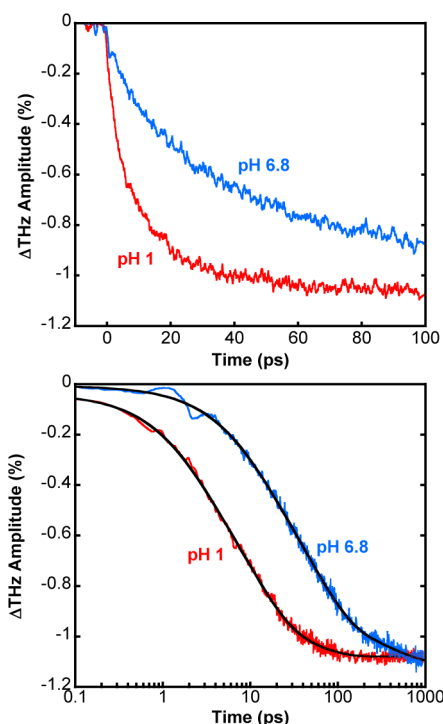


Figure 4. TRTS measurement of Ru(II)phos on SnO₂ at short (upper) and long (lower) time scales in 0.1 M HClO₄ (pH 1, red) and 100 mM potassium phosphate buffer (pH 6.8, blue). Solid black lines are the fitted triexponential functions.

rapid at pH 1 than at pH 6.8. For pH 1, the lifetimes extracted by fitting a convoluted triexponential to TRTS traces were 1.7, 9, and 37 ps, while at pH 6.8 the function generates lifetimes of 7.7, 50, and 435 ps (Table 1). Unlike the case of Ru(II)phos-TiO₂, the overall injection amplitude at pH 6.8 reaches that at pH 1 at a time-delay of 950 ps, despite slower injection kinetics. With SnO₂ there is still a significant driving force for injection even at pH 6.8, allowing for a more complete injection than in the case of TiO₂. Interestingly, the major difference in the injection kinetics between SnO₂ and TiO₂ is in the initial fast component. At pH 6.8, fast injection into TiO₂ occurred with a time constant of 1.2 ps, whereas the “fast” component of injection into SnO₂ occurred with a time constant of 7.7 ps.

Xiang et al.²¹ also probed the ultrafast dynamics of Ru(II)phos injection into SnO₂ using transient absorbance. Looking at samples in air, they observed lifetimes of 4, 30, and 224 ps, with the injection amplitude split uniformly between the three components. Due to different experimental conditions it is difficult to make a direct comparison with this study, however, we note that at pH 6.8 we see somewhat slower injection kinetics. As with TiO₂, this could imply a similar initial injection into nonmobile states, however, more work is needed to confirm this.

3.4. Injection into SnO₂/TiO₂. Back electron transfer is an overwhelming limitation to power conversion efficiencies in WS-DSPECs.²⁵ One potentially promising strategy is to utilize a core/shell electrode where the electron either tunnels through a thin layer of a wide bandgap metal oxide⁹ or proceeds through a “cascade” mechanism wherein the electron is first injected into the conduction band of the shell before relaxing into the conduction band of the core. Recently Meyer and co-workers have demonstrated an enhancement in photocurrent and stability with WS-DSPECs utilizing SnO₂-cores, TiO₂-

shells (hereafter SnO₂/TiO₂) prepared by ALD.^{18,19,51} Because of the offset in conduction band potentials, back electron transfer in these electrodes is slowed by approximately an order of magnitude, though the initial injection kinetics are poorly characterized.

Figure 5 shows a high resolution EDS image of a pair of SnO₂ particles coated with approximately 2.5 ± 0.1 nm of TiO₂

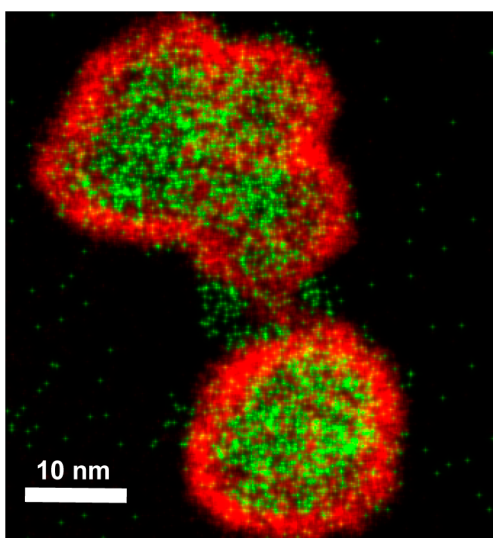


Figure 5. High resolution EDS mapping of SnO₂/TiO₂ particles. Titanium is colored red, and tin is colored green.

using ALD. The TiO₂ shell is conformal and uniform throughout the film. This thickness was chosen to correspond to recent work by Meyer and co-workers.^{18,19,51} Figure S1 shows that addition of the TiO₂ overlayer increases the background scattering, however, when correcting for scattering a nearly identical amount of sensitizer is deposited.

Figure 6 shows the TRTS scans for the sensitized Ru(II)phos-SnO₂/TiO₂ films at pH 1 and pH 6.8. The injection kinetics are markedly different when compared to bare SnO₂. One significant difference is that over the 1 ns time scale of the measurement, the injection amplitude does not reach the same magnitude as with Ru(II)phos-SnO₂. This may reflect slower injection kinetics and/or a loss of driving force related to the presence of the TiO₂ shell.

A second significant difference is the striking feature immediately after time-zero in the TRTS scans of Ru(II)phos-SnO₂/TiO₂. Initially there is an extremely fast change in THz amplitude, indicating a rapid injection component, which decreases in intensity over a few picoseconds before evolving into slower injection dynamics. Due to this feature, the overall dynamics are not well fit using a convoluted triexponential function, but rather require a four-component function to accurately reproduce the initial kinetics. The initial rapid amplitude change is limited by instrument response, while the relatively slower recovery of the THz amplitude occurs with a time constant of 1.4 ps. There are two additional time constants of 98 and 388 ps associated with the increase in carrier generation following the initial feature. One interpretation is that the initial fast injection and decay correspond to injection into mobile TiO₂ states followed by decay into nonmobile states at the SnO₂/TiO₂ interface and/or in the TiO₂ shell. The slow components (98 and 388 ps) may relate to electrons being

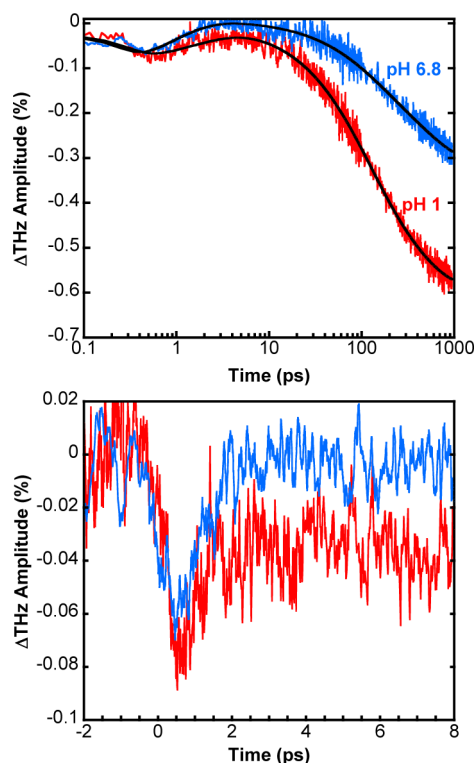


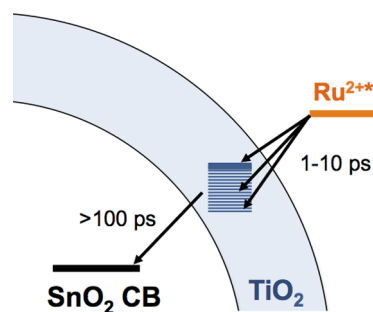
Figure 6. (Upper) TRTS measurement of Ru(II)phos on SnO₂/TiO₂ in 0.1 M HClO₄ (pH 1, red) and 100 mM potassium phosphate buffer (pH 6.8, blue). Solid black lines are the fitted functions described in text. (Lower) Initial time kinetics of Ru(II)phos on SnO₂/TiO₂.

released from nonmobile states and injected into conduction band of the SnO₂ core.

The kinetics are similar at pH 6.8. There is the same instrument response limited rapid injection and amplitude loss as observed at pH 1, however, nearly all the initial amplitude loss is recovered over 1–2 ps. The extracted long time constants (95 and 430 ps) are also very similar to the long time components at pH 1. The similarity in time constants and difference in injection amplitude strongly suggest that in both samples the slow kinetics are related to electron release from nonmobile trap states into the SnO₂ (Scheme 2).

At a TiO₂ thickness of ~2.5 nm, tunneling is unlikely on this time scale,⁵² and thus the injection efficiency is likely controlled

Scheme 2. Proposed injection scheme for Ru(II)phos-TiO₂/SnO₂⁴



⁴The excited dye rapidly injects into the TiO₂-shell. Despite some injection into mobile TiO₂ states, the electrons eventually reside in nonmobile trap states that slowly decay over 100+ ps into the SnO₂.

by the energetics of the TiO_2 . Due to Nernstian behavior, the relative energy difference between the conduction band of TiO_2 and SnO_2 will be pH independent. Assuming that the energy of the nonmobile trap states is also Nernstian, the release kinetics from these states would also be expected to be independent of pH, which is consistent with the observed behavior. As we observed above, injection at pH 1 is significantly more efficient than pH 6.8 because of the additional 340 mV of driving force. A detailed study to better understand the injection and trapping behavior in $\text{SnO}_2/\text{TiO}_2$ films is planned.

4. CONCLUSION

In this paper, we have reported the first TRTS study of four common electrode designs used in WS-DSPECs. By using the same sensitizing and measurement conditions, we are able to directly compare the kinetics between these configurations. Generally, electron injection is more rapid and efficient at pH 1 than at pH 6.8, which is expected based on the increased driving force for injection at pH 1. For both Ru(II)phos-TiO_2 and Ru(II)phos-SnO_2 , the appearance of electrons in the conduction band is significantly slower than indicated by transient absorbance experiments under comparable conditions. This suggests a two-step mechanism in these systems in which some electrons are first injected into nonmobile states before decaying into the conduction band. When the Ru(II)phos-TiO_2 surface is passivated with an overlayer of Al_2O_3 , the overall injection amplitude at 950 ps remains unchanged but a larger fraction of electrons are injected on a sub-picosecond time scale.

A marked change in the injection behavior is observed when a $\text{Ru(II)phos-SnO}_2/\text{TiO}_2$ core/shell architecture is utilized. We observe a rapid injection and decay behavior that we assign to injection into the TiO_2 shell and subsequent relaxation into nonmobile trap states. Electrons in these nonmobile states slowly decay into SnO_2 over hundreds of picoseconds. As expected, the release kinetics from these nonmobile states appears to be largely pH independent. A detailed study into the injection and trapping behavior of core/shell electrodes is planned.

■ ASSOCIATED CONTENT

Supporting Information

The Supporting Information is available free of charge on the ACS Publications website at DOI: 10.1021/acs.jpcc.6b00749.

Steady-state UV-vis of the various film configurations (PDF)

■ AUTHOR INFORMATION

Corresponding Authors

*E-mail: tem5@psu.edu.

*E-mail: charles.schmittenmaer@yale.edu.

Author Contributions

[†]J.R.S. and N.S.M. contributed equally.

Notes

The authors declare no competing financial interest.

■ ACKNOWLEDGMENTS

The authors thank Jennifer Gray for her assistance in collecting STEM images and Bangzhi Liu for his help with the ALD experiments. This work was supported by the Office of Basic Energy Sciences, Division of Chemical Sciences, Geosciences,

and Energy Biosciences, Department of Energy, under Contracts DE-FG02-07ER15911 and DE-FG02-07ER15909 as well as by a generous donation from the TomKat Charitable Trust. N.S.M. thanks the National Science Foundation for support as a graduate fellow under Grant DGE1255832. Instrumentation and facilities used in this project were supported by the Pennsylvania State University Materials Research Institute Nanofabrication Laboratory under National Science Foundation Cooperative Agreement ECS-0335765.

■ REFERENCES

- (1) Moore, G. F.; Brudvig, G. W. Energy Conversion in Photosynthesis: a Paradigm for Solar Fuel Production. *Annu. Rev. Condens. Matter Phys.* **2011**, *2*, 303–327.
- (2) McEvoy, J.; Brudvig, G. Water-Splitting Chemistry of Photosystem II. *Chem. Rev.* **2006**, *106*, 4455–4483.
- (3) Asbury, J. B.; Hao, E.; Wang, Y.; Ghosh, H. N.; Lian, T. Ultrafast Electron Transfer Dynamics From Molecular Adsorbates to Semiconductor Nanocrystalline Thin Films. *J. Phys. Chem. B* **2001**, *105*, 4545–4557.
- (4) Milot, R. L.; Schmittenmaer, C. A. Electron Injection Dynamics in High-Potential Porphyrin Photoanodes. *Acc. Chem. Res.* **2015**, *48*, 1423–1431.
- (5) Swierk, J. R.; Mallouk, T. E. Design and Development of Photoanodes for Water-Splitting Dye-Sensitized Photoelectrochemical Cells. *Chem. Soc. Rev.* **2013**, *42*, 2357–2387.
- (6) Brennan, B. J.; Durrell, A. C.; Koepf, M.; Crabtree, R. H.; Brudvig, G. W. Towards Multielectron Photocatalysis: a Porphyrin Array for Lateral Hole Transfer and Capture on a Metal Oxide Surface. *Phys. Chem. Chem. Phys.* **2015**, *17*, 12728–12734.
- (7) Hanson, K.; Brenneman, M. K.; Ito, A.; Luo, H.; Song, W.; Parker, K. A.; Ghosh, R.; Norris, M. R.; Glasson, C. R. K.; Concepcion, J. J.; et al. Structure-Property Relationships in Phosphonate-Derivatized, RuII Polypyridyl Dyes on Metal Oxide Surfaces in an Aqueous Environment. *J. Phys. Chem. C* **2012**, *116*, 14837–14847.
- (8) Youngblood, W. J.; Lee, S.-H. A.; Kobayashi, Y.; Hernandez-Pagan, E. A.; Hoertz, P. G.; Moore, T. A.; Moore, A. L.; Gust, D.; Mallouk, T. E. Photoassisted Overall Water Splitting in a Visible Light-Absorbing Dye-Sensitized Photoelectrochemical Cell. *J. Am. Chem. Soc.* **2009**, *131*, 926–927.
- (9) Lee, S.-H. A.; Zhao, Y.; Hernandez-Pagan, E. A.; Blasdel, L.; Youngblood, W. J.; Mallouk, T. E. Electron Transfer Kinetics in Water Splitting Dye-Sensitized Solar Cells Based on Core-Shell Oxide Electrodes. *Faraday Discuss.* **2012**, *155*, 165–176.
- (10) Zhao, Y.; Swierk, J. R.; Megiatto, J. D.; Sherman, B.; Youngblood, W. J.; Qin, D.; Lentz, D. M.; Moore, A. L.; Moore, T. A.; Gust, D.; et al. Improving the Efficiency of Water Splitting in Dye-Sensitized Solar Cells by Using a Biomimetic Electron Transfer Mediator. *Proc. Natl. Acad. Sci. U. S. A.* **2012**, *109*, 15612–15615.
- (11) Swierk, J. R.; McCool, N. S.; Saunders, T. P.; Barber, G. D.; Strayer, M. E.; Vargas-Barbosa, N. M.; Mallouk, T. E. Photovoltage Effects of Sintered IrO_2 Nanoparticle Catalysts in Water-Splitting Dye-Sensitized Photoelectrochemical Cells. *J. Phys. Chem. C* **2014**, *118*, 17046–17053.
- (12) Swierk, J. R.; Méndez-Hernández, D. D.; McCool, N. S.; Liddell, P.; Terazono, Y.; Pahk, I.; Tomlin, J. J.; Oster, N. V.; Moore, T. A.; Moore, A. L.; et al. Metal-Free Organic Sensitizers for Use in Water-Splitting Dye-Sensitized Photoelectrochemical Cells. *Proc. Natl. Acad. Sci. U. S. A.* **2015**, *112*, 1681–1686.
- (13) Gao, Y.; Ding, X.; Liu, J.; Wang, L.; Lu, Z.; Li, L.; Sun, L. Visible Light Driven Water Splitting in a Molecular Device with Unprecedentedly High Photocurrent Density. *J. Am. Chem. Soc.* **2013**, *135*, 4219–4222.
- (14) Li, L.; Duan, L.; Xu, Y.; Gorlov, M.; Hagfeldt, A.; Sun, L. A Photoelectrochemical Device for Visible Light Driven Water Splitting by a Molecular Ruthenium Catalyst Assembled on Dye-Sensitized Nanostructured TiO_2 . *Chem. Commun.* **2010**, *46*, 7307–7309.

- (15) Li, F.; Fan, K.; Xu, B.; Gabrielson, E.; Daniel, Q.; Li, L.; Sun, L. Organic Dye-Sensitized Tandem Photoelectrochemical Cell for Light Driven Total Water Splitting. *J. Am. Chem. Soc.* **2015**, *137*, 9153–9159.
- (16) Moore, G. F.; Blakemore, J. D.; Milot, R. L.; Hull, J. F.; Song, H.-E.; Cai, L.; Schmittenmaer, C. A.; Crabtree, R. H.; Brudvig, G. W. A Visible Light Water-Splitting Cell with a Photoanode Formed by Codeposition of a High-Potential Porphyrin and an Iridium Water-Oxidation Catalyst. *Energy Environ. Sci.* **2011**, *4*, 2389–2392.
- (17) Poddutoori, P. K.; Thomsen, J. M.; Milot, R. L.; Sheehan, S. W.; Negre, C. F. A.; Garapati, V. K. R.; Schmittenmaer, C. A.; Batista, V. S.; Brudvig, G. W.; van der Est, A. Interfacial Electron Transfer in Photoanodes Based on Phosphorus(V) Porphyrin Sensitizers Co-Deposited on SnO₂ with the Ir(III)Cp* Water Oxidation Precatalyst. *J. Mater. Chem. A* **2015**, *3*, 3868–3879.
- (18) Alibabaei, L.; Brennaman, M. K.; Norris, M. R.; Kalanyan, B.; Song, W.; Losego, M. D.; Concepcion, J. J.; Binstead, R. A.; Parsons, G. N.; Meyer, T. J. Solar Water Splitting in a Molecular Photoelectrochemical Cell. *Proc. Natl. Acad. Sci. U. S. A.* **2013**, *110*, 20008–20013.
- (19) Sherman, B. D.; Ashford, D. L.; Lapidés, A. M.; Sheridan, M. V.; Wee, K.-R.; Meyer, T. J. Light-Driven Water Splitting with a Molecular Electroassembly-Based Core/Shell Photoanode. *J. Phys. Chem. Lett.* **2015**, *6*, 3213–3217.
- (20) Michaux, K. E.; Gambardella, A. A.; Alibabaei, L.; Ashford, D. L.; Sherman, B. D.; Binstead, R. A.; Meyer, T. J.; Murray, R. W. Visible Photoelectrochemical Water Splitting Based on a Ru(II) Polypyridyl Chromophore and Iridium Oxide Nanoparticle Catalyst. *J. Phys. Chem. C* **2015**, *119*, 17023–17027.
- (21) Xiang, X.; Fielden, J.; Rodríguez-Córdoba, W.; Huang, Z.; Zhang, N.; Luo, Z.; Musaev, D. G.; Lian, T.; Hill, C. L. Electron Transfer Dynamics in Semiconductor–Chromophore–Polyoxometalate Catalyst Photoanodes. *J. Phys. Chem. C* **2013**, *117*, 918–926.
- (22) Fielden, J.; Sumliner, J. M.; Han, N.; Geletii, Y. V.; Xiang, X.; Musaev, D. G.; Lian, T.; Hill, C. L. Water Splitting with Polyoxometalate-Treated Photoanodes: Enhancing Performance Through Sensitizer Design. *Chem. Sci.* **2015**, *6*, 5531–5543.
- (23) Creutz, C.; Sutin, N. Reaction of Tris(bipyridine)ruthenium(III) with Hydroxide and its Application in a Solar Energy Storage System. *Proc. Natl. Acad. Sci. U. S. A.* **1975**, *72*, 2858–2862.
- (24) Swierk, J. R.; McCool, N. S.; Saunders, T. P.; Barber, G. D.; Mallouk, T. E. Effects of Electron Trapping and Protonation on the Efficiency of Water-Splitting Dye-Sensitized Solar Cells. *J. Am. Chem. Soc.* **2014**, *136*, 10974–10982.
- (25) Swierk, J. R.; McCool, N. S.; Mallouk, T. E. Dynamics of Electron Recombination and Transport in Water-Splitting Dye-Sensitized Photoanodes. *J. Phys. Chem. C* **2015**, *119*, 13858–13867.
- (26) Milot, R. L.; Moore, G. F.; Crabtree, R. H.; Brudvig, G. W.; Schmittenmaer, C. A. Electron Injection Dynamics From Photoexcited Porphyrin Dyes Into SnO₂ and TiO₂ Nanoparticles. *J. Phys. Chem. C* **2013**, *117*, 21662–21670.
- (27) Giokas, P. G.; Miller, S. A.; Hanson, K.; Norris, M. R.; Glasson, C. R. K.; Concepcion, J. J.; Bettis, S. E.; Meyer, T. J.; Moran, A. M. Spectroscopy and Dynamics of Phosphonate-Derivatized Ruthenium Complexes on TiO₂. *J. Phys. Chem. C* **2013**, *117*, 812–824.
- (28) Beard, M. C.; Turner, G. M.; Schmittenmaer, C. A. Transient Photoconductivity in GaAs as Measured by Time-Resolved Terahertz Spectroscopy. *Phys. Rev. B: Condens. Matter Mater. Phys.* **2000**, *62*, 15764–15777.
- (29) Gillaizeau-Gauthier, I.; Odobel, F.; Alebbi, M.; Argazzi, R.; Costa, E.; Bignozzi, C. A.; Qu, P.; Meyer, G. J. Phosphonate-Based Bipyridine Dyes for Stable Photovoltaic Devices. *Inorg. Chem.* **2001**, *40*, 6073–6079.
- (30) Ito, S.; Chen, P.; Comte, P.; Nazeeruddin, M. K.; Liska, P.; Péchy, P.; Grätzel, M. Fabrication of Screen-Printing Pastes From TiO₂ Powders for Dye-Sensitized Solar Cells. *Prog. Photovoltaics* **2007**, *15*, 603–612.
- (31) Hanson, K.; Brennaman, M. K.; Luo, H.; Glasson, C. R. K.; Concepcion, J. J.; Song, W.; Meyer, T. J. Photostability of Phosphonate-Derivatized, Ru(II) Polypyridyl Complexes on Metal Oxide Surfaces. *ACS Appl. Mater. Interfaces* **2012**, *4*, 1462–1469.
- (32) Turner, G. M.; Beard, M. C.; Schmittenmaer, C. A. Carrier Localization and Cooling in Dye-Sensitized Nanocrystalline Titanium Dioxide. *J. Phys. Chem. B* **2002**, *106*, 11716–11719.
- (33) Baxter, J. B.; Schmittenmaer, C. A. Conductivity of ZnO Nanowires, Nanoparticles, and Thin Films Using Time-Resolved Terahertz Spectroscopy. *J. Phys. Chem. B* **2006**, *110*, 25229–25239.
- (34) Beard, M. C.; Turner, G. M.; Schmittenmaer, C. A. Subpicosecond Carrier Dynamics in Low-Temperature Grown GaAs as Measured by Time-Resolved Terahertz Spectroscopy. *J. Appl. Phys.* **2001**, *90*, 5915–5923.
- (35) Nemes, C. T.; Koenigsmann, C.; Schmittenmaer, C. A. Functioning Photoelectrochemical Devices Studied with Time-Resolved Terahertz Spectroscopy. *J. Phys. Chem. Lett.* **2015**, *6*, 3257–3262.
- (36) Cook, D. J.; Hochstrasser, R. M. Intense Terahertz Pulses by Four-Wave Rectification in Air. *Opt. Lett.* **2000**, *25*, 1210–1212.
- (37) Bartel, T.; Gaal, P.; Reimann, K.; Woerner, M.; Elsaesser, T. Generation of Single-Cycle THz Transients with High Electric-Field Amplitudes. *Opt. Lett.* **2005**, *30*, 2805–2807.
- (38) Wu, Q.; Zhang, X. C. Free-Space Electro-Optic Sampling of Terahertz Beams. *Appl. Phys. Lett.* **1995**, *67*, 3523–3525.
- (39) Asbury, J. B.; Wang, Y. Q.; Hao, E.; Ghosh, H. N.; Lian, T. Evidences of Hot Excited State Electron Injection From Sensitizer Molecules to TiO₂ Nanocrystalline Thin Films. *Res. Chem. Intermed.* **2001**, *27*, 393–406.
- (40) Pijpers, J. J. H.; Ulbricht, R.; Derossi, S.; Reek, J. N. H.; Bonn, M. Picosecond Electron Injection Dynamics in Dye-Sensitized Oxides in the Presence of Electrolyte. *J. Phys. Chem. C* **2011**, *115*, 2578–2584.
- (41) Furube, A.; Katoh, R.; Hara, K.; Murata, S.; Arakawa, H.; Tachiya, M. Ultrafast Stepwise Electron Injection From Photoexcited Ru-Complex Into Nanocrystalline ZnO Film via Intermediates at the Surface. *J. Phys. Chem. B* **2003**, *107*, 4162–4166.
- (42) Furube, A.; Katoh, R.; Yoshihara, T.; Hara, K.; Murata, S.; Arakawa, A.; Tachiya, M. Ultrafast Direct and Indirect Electron-Injection Processes in a Photoexcited Dye-Sensitized Nanocrystalline Zinc Oxide Film: the Importance of Exciplex Intermediates at the Surface. *J. Phys. Chem. B* **2004**, *108*, 12583–12592.
- (43) Knauf, R. R.; Brennaman, M. K.; Alibabaei, L.; Norris, M. R.; Dempsey, J. L. Revealing the Relationship Between Semiconductor Electronic Structure and Electron Transfer Dynamics at Metal Oxide–Chromophore Interfaces. *J. Phys. Chem. C* **2013**, *117*, 25259–25268.
- (44) Listorti, A.; O'Regan, B.; Durrant, J. Electron Transfer Dynamics in Dye-Sensitized Solar Cells. *Chem. Mater.* **2011**, *23*, 3381–3399.
- (45) Hanson, K.; Losego, M. D.; Kalanyan, B.; Ashford, D. L.; Parsons, G. N.; Meyer, T. J. Stabilization of [Ru(Bpy)₂(4,4'-(PO₃H₂)Bpy)]²⁺ on Mesoporous TiO₂ with Atomic Layer Deposition of Al₂O₃. *Chem. Mater.* **2013**, *25*, 3–5.
- (46) Hanson, K.; Losego, M. D.; Kalanyan, B.; Parsons, G. N.; Meyer, T. J. Stabilizing Small Molecules on Metal Oxide Surfaces Using Atomic Layer Deposition. *Nano Lett.* **2013**, *13*, 4802–4809.
- (47) Lapidés, A. M.; Sherman, B. D.; Brennaman, M. K.; Dares, C. J.; Skinner, K. R.; Templeton, J. L.; Meyer, T. J. Synthesis, Characterization, and Water Oxidation by a Molecular Chromophore-Catalyst Assembly Prepared by Atomic Layer Deposition. the “Mummy” Strategy. *Chem. Sci.* **2015**, *6*, 6398–6406.
- (48) Prasittichai, C.; Avila, J. R.; Farha, O. K.; Hupp, J. T. Systematic Modulation of Quantum (Electron) Tunneling Behavior by Atomic Layer Deposition on Nanoparticulate SnO₂ and TiO₂ Photoanodes. *J. Am. Chem. Soc.* **2013**, *135*, 16328–16331.
- (49) Ai, X.; Anderson, N. A.; Guo, J.; Lian, T. Electron Injection Dynamics of Ru Polypyridyl Complexes on SnO₂ Nanocrystalline Thin Films. *J. Phys. Chem. B* **2005**, *109*, 7088–7094.
- (50) Tiwana, P.; Docampo, P.; Johnston, M. B.; Snaith, H. J.; Herz, L. M. Electron Mobility and Injection Dynamics in Mesoporous ZnO, SnO₂, and TiO₂ Films Used in Dye-Sensitized Solar Cells. *ACS Nano* **2011**, *5*, 5158–5166.

(51) Wee, K.-R.; Sherman, B. D.; Brennaman, M. K.; Sheridan, M. V.; Nayak, A.; Alibabaei, L.; Meyer, T. J. An Aqueous, Organic Dye Derivatized SnO₂/TiO₂ Core/Shell Photoanode. *J. Mater. Chem. A* **2016**, *4*, 2969.

(52) Li, T. T. T.; Weaver, M. J. Intramolecular Electron Transfer at Metal Surfaces. 4. Dependence of Tunneling Probability Upon Donor-Acceptor Separation Distance. *J. Am. Chem. Soc.* **1984**, *106*, 6107–6108.